ACS APPLIED MATERIALS & INTERFACES

Research Article

www.acsami.org

Depth-Resolved Multispectral Sub-Surface Imaging Using Multifunctional Upconversion Phosphors with Paramagnetic Properties

Zaven Ovanesyan,[*,†] L. Christopher Mimun,[†] Gangadharan Ajith Kumar,[†] Brian G. Yust,[‡] Chamath Dannangoda,[§] Karen S. Martirosyan,[§] and Dhiraj K. Sardar[†]

[†]Department of Physics and Astronomy, The University of Texas at San Antonio, San Antonio, Texas 78249, United States
[‡]Department of Physics, University of Texas at Rio Grande Valley, Edinburg, Texas 78539, United States
[§]Department of Physics and Astronomy, University of Texas at Rio Grande Valley, Brownsville, Texas 78520, United States

ABSTRACT: Molecular imaging is very promising technique used for surgical guidance, which requires advancements related to properties of imaging agents and subsequent data retrieval methods from measured multispectral images. In this article, an upconversion material is introduced for subsurface near-infrared imaging and for the depth recovery of the material embedded below the biological tissue. The results confirm significant correlation between the analytical depth estimate of the material under the tissue and the measured ratio of emitted light from the material at two different wavelengths. Experiments with biological tissue samples demonstrate depth resolved imaging using the rare earth doped multifunctional phosphors. In vitro tests reveal no significant toxicity, whereas the magnetic measurements of the phosphors show that the particles are suitable as magnetic resonance imaging agents. The confocal imaging of fibroblast cells with these phosphors reveals their potential for in vivo imaging. The depth-resolved imaging technique with such phosphors has broad implications for real-time intraoperative surgical guidance.

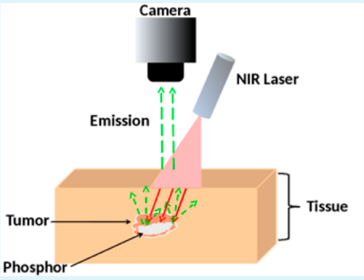

KEYWORDS: *upconversion, imaging, light propagation in tissue, spectroscopy, magnetic properties*

1. INTRODUCTION

Recent advancements in nanotechnology have increased the demand of fluorescence bioimaging in biomedical applications.[1,2] In direct or indirect light induced imaging and therapy, light provides new venues for noninvasive detection, diagnosis, and improving resection of target tissue during the therapy. Direct light-based imaging and therapy relies on X-rays, γ-rays, and other high energy photons that can be harmful for the tissue because of ionizing effects. On the contrary, indirect infrared (IR) and near-infrared light (NIR) provide a unique nonionizing method to noninvasively investigate the properties of tissue due to good transparency in NIR spectrum, low photon energy, high penetration depth, localized delivery and low tissue damage. The most common biomarkers used in both direct and indirect imaging technologies are based on organic fluorophores and quantum dots. For instance, fluorescence imaging can be used in intraoperative image-guided resection of tumors.[3,4] Fluorescence detection is capable of providing complementary information to the conventional imaging methods such as magnetic resonance imaging (MRI), ultrasound (US) and computed tomography (CT) that reveal structural properties of tissue. Particularly, fluorescence imaging can provide molecular or functional information on tissue, which has been conjugated with a fluorophore or a quantum dot.[5−8]

Recent experimental developments of fluorescence diffuse optical tomography (fDOT) of tissue have been related with multispectral approaches.[9,10] In the fDOT-based experiments, the information about the depth of fluorescence source can be obtained by calculating the ratio of transmitted fluorescence signal trough the tissue at two different wavelengths.[11−14] As a consequence, there is no need for using the time-resolved or frequency domain information for such fDOT systems. The emission spectra of fluorescence agents can be accessed through fiber-optic based spectroscopy or multispectral imaging. The main challenge in spectral coverage of the fluorescence agent is related to the large tissue attenuation in biological samples within blue end of the optical properties of tissue. Thus, in order to properly retrieve fluorescence spectrum, fluorophores must have wide emission bandwidth and simultaneously overlap with the large optical contrast of the tissue.[15]

Lately, there has been a lot of interest in the application of multifunctional materials for several biomedical applications.[16,17] Material with multiple functionalities can provide more information than conventional materials with single functionalities. For example, in the medical imaging industry several imaging techniques such as CT (based on X-ray), MRI (based on magnetic features), and fluorescence (based on organic dyes, quantum dots), etc., have been well-established. Though each of these techniques has their own advantages and disadvantages, the major difficulty is the lack of multimodal imaging features.

Received: July 17, 2015
Accepted: August 31, 2015
Published: August 31, 2015

DOI: 10.1021/acsami.5b06491
ACS Appl. Mater. Interfaces 2015, 7, 21465−21471

To circumvent these major issues, as well as to overcome the other drawbacks such as photobleaching of the dyes, toxicity, and size tuning of the quantum dots, rare earth doped phosphors are brought as a new multifunctional imaging agents with far less toxicity and several other advantages compared to all other imaging agents.[18] These phosphors have a nonlinear excitation power-dependence, and remain photostable even when they are intensively illuminated, thus enabling longer experimentation. Also, they have multiple excitation and emission bands in the visible and NIR (I, II, III biological window) regions where the absorption and emission depend only on the dopant. This makes phosphors distinct from quantum dots where the spectroscopic properties depend on size. Moreover, the rare earth phosphors have strong NIR excitation and emission properties, which facilitate deep tissue imaging with far better contrast.

In this paper, we establish Yb and Er codoped Gd_2O_2S as a contrast agent with multiple features such as emission under NIR excitation, as well as magnetic properties. Following the optical and magnetic characterizations of the material, from the experimentally collected emission data we estimate a depth of the upconverting phosphor embedded beneath the chicken breast tissue with the fDOT technique. We use analytic expression to calculate gamma value e.g. the ratio of two emission intensities from the phosphor at two different wavelengths and study its dependence on phosphor's depth. We then compare theoretical predictions for gamma with the fDOT experimental measurements. Our results reveal linear dependence of gamma on depth, which is in agreement with recent florescence subsurface imaging studies.[13,19] Further, we also perform NIR confocal imaging experiments to show the cellular uptake of the phosphor particles.

2. METHODS

2.1. Phosphor Preparation and Characterization. Yb and Er co-doped Gd_2O_2S phosphor was prepared by the high-temperature solid-state flux fusion method as reported previously.[20] The starting materials were Gd_2O_3, Yb_2O_3, Er_2O_3 (Sigma-Aldrich, all 99.999%, USA), S, and flux Na_2CO_3, K_3PO_4 (Sigma-Aldrich, 99.99%, USA). Based on our previous experiments the Yb: Er molar concentration ratio was selected as 8:1 for the brightest emission. After mixing all the precursors using an agate mortar, the mix was fired in a muffle furnace at 1423 K for 60 min. After cooling down, the product was taken out from the furnace, crushed well, and washed with distilled water 6 times to eliminate the unreacted sulfur. Finally, the powder was washed with mild hydrochloric acid. The washed powder was subsequently dried at 373 K for an hour to obtain the final product.

The powder X-ray diffraction (XRD) was performed at 40 kV and 30 mA in the parallel beam configuration using the Ultima IV X-ray diffractometer (RIGAKU, Japan) with Cu Kα ($\lambda = 1.5$ A). The morphology of the samples was observed using the field emission scanning transmission electron microscope (FE-STEM) S5500 (Hitachi, Japan) operated at 30 kV in secondary electron mode.

Fluorescence spectrum of the phosphor was obtained using QuantaMaster 51 spectrofluorometer (Photon Technology International Inc. USA) under the 980 nm laser excitation.

Magnetic properties were determined by using the multifunctional instrument cryogen-free cryocooler-based physical property measurement system (PPMS) EverCool−II (Quantum Design, USA). The hysteresis loops of magnetization were measured at room temperature and 5 K under a maximum applied field of ±9 T. Field-cooling (FC) magnetization curves were measured in the temperature range 1.9−300 K using field of 100 Oe.

2.2. Imaging Experiments. *2.2.1. Penetration Depth Experiments.* The samples with chicken breast tissue were prepared in the biophotonics lab of the University of Texas at San Antonio. The chicken breast was purchased from a local supermarket with no additives or preservatives and were sliced at various thickness (0.9 mm, 1.7 mm, 2.9 mm, 3.9 mm). The sliced pieces were placed between two microscope glass slides and taped together (Figure 1a).

The schematic representation of the experimental setup used for fluorescence imaging study is shown in Figure 1b. The phosphors were placed beneath the tissue sample and were excited with an expanded 980 nm diode laser beam (Axcel Photonics, B2−980−3000−15A, USA) with varying fluence, which was set by a power controller (Thorlabs LM74S2 Driver, Thorlabs LDC2000−2A Laser Diode Controller, USA). The reflected fluorescence intensity signal from the phosphors was guided through a bandpass filter (Thorlabs, USA) before entering the charge coupled device (CCD) camera (Hamamatsu C3077−79, Japan). The camera was connected to a computer and operated by the Hamamatsu imaging software. The power of the laser delivered on the surface of the sample was around 0.33 W, whereas the diameter of the corresponding excitation laser beam was around 1.0 cm. The experiment was performed with beam expander to spread the laser light distribution on the surface evenly. The power per unit area was controlled by expanding the illumination beam or increasing the fluence of the excitation beam.

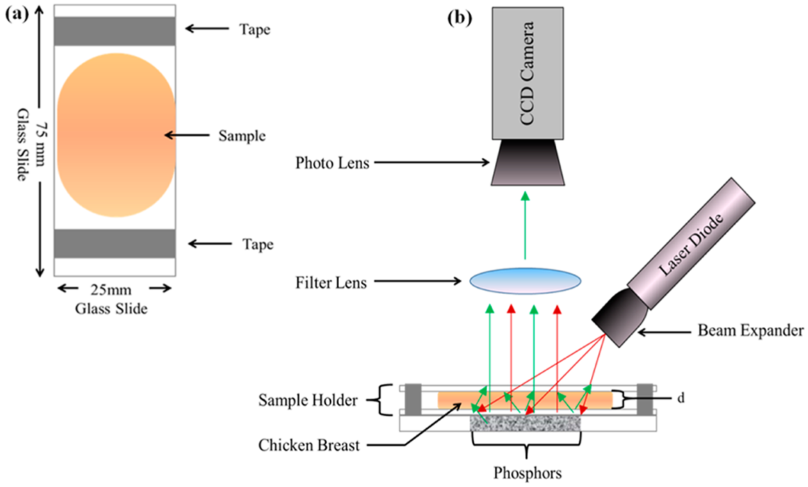

Figure 1. (a) Top view of the chicken breast sample and holder geometry. The samples were placed between two microscope slides, with tape to keep the slides bounded to the sample. (b) Schematics showing the main optical components of CCD-based imaging systems, illustrating that imaging is performed in epi-illumination (reflectance) mode. The sample is illuminated by a 980 nm laser beam. The laser light propagates in the sample as a diffuse light and excites the phosphor under the chicken breast tissue. The diffused emission signal is retrieved by CCD camera via series of multispectral image acquisitions.

CCD camera acquired 640 by 480 pixel size fluorescence images at 30 frames per second. The region of interest (ROI) from pixels within a 3 × 3 square was selected on these images in order to calculate the fluorescence intensity. The following formula was used to calculate the total fluorescence (TF) within the ROI: TF = integrated density − (area of selected ROI·mean fluorescence of background reading).[21] The background fluorescence reading was chosen within the 3 × 3 square area further from the sample.

2.2.2. Confocal Cell Imaging. For the confocal experiments, we used fibroblast cells (L929). Phosphors at a concentration of 200 μgm^{-1}L^{-1} were injected into growth media by vigorous vortexing, and the cells were incubated in it for 24 h. Subsequently, the cells were washed three times with phosphate buffered saline solution to remove excess phosphors. The dyes used for coloring the cell components were DAPI (nuclei), and Alexa Fluor 647 phalloidin (cytoplasm). The samples were then mounted on microscope slides for imaging with Zeiss 710 multiphoton confocal imaging system. The phosphors were excited with a pulsed titanium sapphire laser at 980 nm with the green emission collected for imaging. To confirm the uptake of the phosphors by cells, we performed colocalization analysis of the raw image data with the imaging software Imaris.

2.3. Analytical Model. The analytical model used in this work was based on the approach introduced by Leblond et al.[13] and recently enhanced by Koltse et al.[19] In this model, the solution for light transport in tissue was used within infinite medium approach and point-like fluorescent inclusion limit, which provides an analytical solution in the form of eq 1. The gamma in this formula contains information related to the spectral deformation because of the blue shift of emission spectra as it propagates through the tissue

$$\ln \Gamma_\infty = \left[\frac{1}{\delta^{\lambda_2}} - \frac{1}{\delta^{\lambda_1}}\right] d + \ln \frac{D^{\lambda_2}}{D^{\lambda_1}} \tag{1}$$

where the diffusion constant is expressed by following expression

$$D^\lambda = \frac{1}{3(\mu_a^\lambda + \mu_s'^\lambda)} \tag{2}$$

and the penetration depth is given by

$$\delta^\lambda = \sqrt{\frac{D^\lambda}{\mu_a^\lambda}} \tag{3}$$

Both eq 2 and 3 are functions of the reduced scattering, $\mu_s'^\lambda$, and the absorption coefficient, μ_a^λ for a specific wavelength. For the optical properties of chicken breast tissue, we used available experimental data.[22] Interestingly, eq 1 is of the linear form, in which the logarithm of fluorescence ratio at two wavelengths linearly depends on the depth of fluorescent source under the tissue. It has been demonstrated that this model can be used not only in pointlike fluorescence depth estimation but also in topographic mapping of subsurface fluorescence depth.[23] This depth retrieval technique requires reduced scattering and absorption coefficients of the tissue to be known a priori. Table 1 demonstrates optical properties of chicken breast tissue for two different wavelengths.

Table 1. Optical Properties of Chicken Breast Tissue Taken from Ref 22[a]

λ (nm)	$\mu_{s'}$ (cm^{-1})	μ_a (cm^{-1})
545	4.7126	0.5987
560	4.7134	0.4311

[a] First column represents wavelength, second and third columns correspond to reduced scattering and absorption coefficients, respectively.

3. RESULTS AND DISCUSSION

3.1. Phase and Morphology. The XRD data obtained for the phosphor sample is shown in Figure 2. The data is in perfect match with standard powder peak positions of the hexagonal phase (JCPDS Card No.26−1422). The XRD results reveal that the phosphor is crystallized in the hexagonal phase with cell parameters $a = b = 0.3852$ nm, $c = 0.6567$ nm. FE-STEM micrographs obtained from different locations show that the material mostly crystallized in hexagonal shape (Figure 3a) with average particle size of 3 to 4 μm. According to the dynamic light scattering measurements (Figure 3b) the average particle size is estimated to be 3 μm.

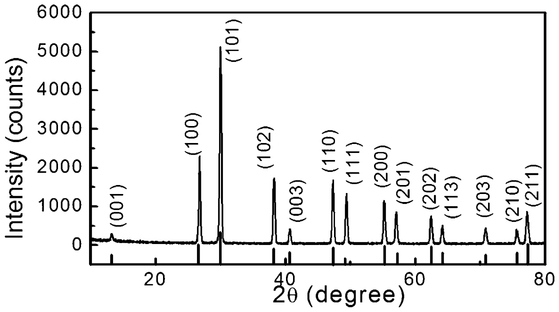

Figure 2. XRD pattern of the Gd_2O_2S: Yb/Er sample. Vertical line shows the standard peak positions of the Gd_2O_2S (JCPD File No 26−1422).

3.2. Optical Properties. The upconversion spectrum of the phosphor (Figure 4) has been collected under 980 nm excitation. The spectrum shows well resolved emission lines in the green and red region with several Stark components at 524, 527, 533, 548, 554 nm (for green) and 655, 661, 663, 669 nm (for red). The 533 and 548 nm transition bands are assigned to $^2H_{11/2} \rightarrow {}^4I_{15/2}$ and $^4S_{3/2} \rightarrow {}^4I_{15/2}$, whereas the 660 nm band is assigned to $^4F_{9/2} \rightarrow {}^4I_{15/2}$ transition as shown in Figure 4. The green emission is 2.4 times stronger than red and their peak emission wavelengths are at 548 and 669 nm. Also, their fluorescence branching ratios are 60 and 37.3%, respectively, for green and red emission.

3.3. Magnetic Properties. We have investigated the room-temperature and low-temperature (5 K) magnetic properties of the phosphor using a vibrating sample magnetometer and the magnetization curve as shown in Figure 5a. The room-temperature and 5 K magnetization curve are almost linear indicating the paramagnetic nature of the material. Magnetization at 9 T for the low temperature hysteresis curve is close to 130 emu/g, which is 13 times larger than the room temperature magnetization (10 emu/g). Magnetic moment per particle has been estimated by fitting the magnetization curve with Langevin function,[24] and the values obtained are 2095 and 20887 μ_B, respectively, at room temperature and 5 K. From the nature of the curve, the Gd_2O_2S:Yb/Er exhibit magnetic properties, which is due to the presence of the paramagnetic ion Gd^{3+} that has larger number of unpaired electrons in the outer orbital. The exponential decay type behavior of the field cooling (FC) studies (Figure 5b) also supports the paramagnetic nature of the material.

3.4. Penetration Depth Studies. The penetration depth experiment has been conducted at the biophotonics lab using chicken breast tissue. The chicken breast tissue samples are placed on top of the sealed phosphors below the CCD camera using the experimental setup shown in Figure 1b. The Gd_2O_2S:Yb/Er spectra are measured at a given depth by using different samples. A 980 nm diode laser of maximum 800 mA with excitation power density per unit area 0.42 W cm^{-2} is used to excite the Gd_2O_2S:Yb/Er in the sample. Images within two

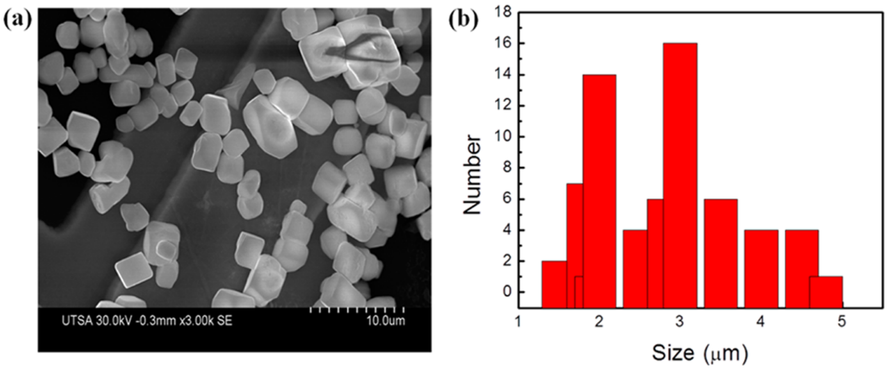

Figure 3. (a) Scanning electron microscope (SEM) micrograph of the Gd_2O_2S: Yb(8)/Er(1) phosphor powder; (b) particle size distribution (PSD).

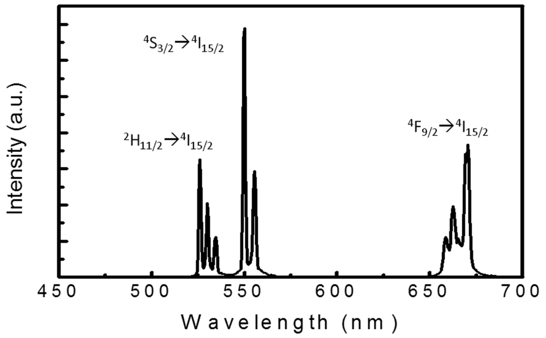

Figure 4. Upconversion emission spectra of Gd_2O_2S; Yb(8)/Er(1) phosphor under 980 nm laser excitation. Assigned peaks correspond to 533, 548, and 660 nm transition bands, respectively.

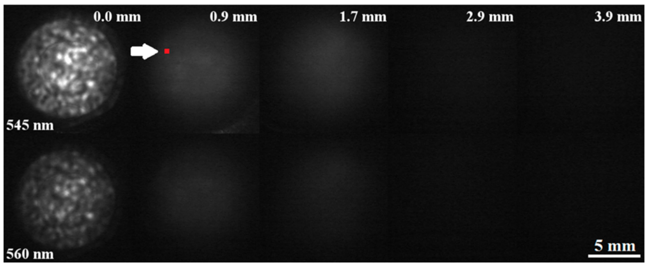

Figure 6. Processed images of the sample with chicken breast tissue and phosphors acquired by CCD-based imaging system. The emission signal for all depths was stronger for 545 nm centered wavelength compared to the emission signal for 560 nm wavelength. White arrow indicates on ROI (filled red square) where the fluorescence intensity was calculated within images.

different wavelength bands are acquired with the CCD camera. Each acquisition captured a 2D image within 5 nm spectral resolution using band-pass filters with 545 and 560 nm central wavelengths under laser light exposure. These wavelength ranges are selected to cover the region of interest of the main spectral features of Gd_2O_2S:Yb/Er. Thus, each 2D image contains spatial (x, y) information within specific wavelength range, and each spatial (x, y) coordinate of a pixel corresponds to a location in the sample. The pixel size is 11.5 μm (horizontal) × 13.5 μm (vertical). The corresponding emission spectra are retrieved from these images by calculating the average intensity of pixels within a 3 × 3 square ROI shown in Figure 6. The average intensity from the images are calculated using ImageJ software in order to interpret the degree of spectral deformations as a function of depth. The corresponding gamma ratio is calculated at each depth. Calculated gamma is then normalized by the gamma at 0 mm depth for a given dual wavelength combination in order to minimize the reflectance spectra from the laser and maximize the fluorescence spectra.

3.4.1. Gamma and Depth Predictions. Figure 7a shows that experimental results for gamma values are in agreement with theory until 4 mm depth. Figure 7b represents estimated depth from the experimental measurements and optical properties of chicken breast tissue (blue triangles) and actual depth of phosphors under the tissue (red triangles). The gamma results for the corresponding wavelength pair of λ_1 = 545 nm and

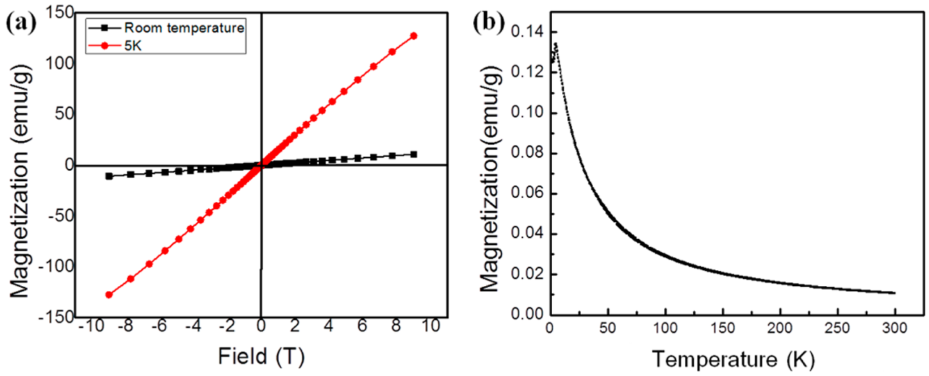

Figure 5. (a) Magnetization of Gd_2O_2S:Yb(8)/Er(1) at room and low temperature. The straight line shows the Langevin fitting with experimental data; (b) field cooling (FC) curve.

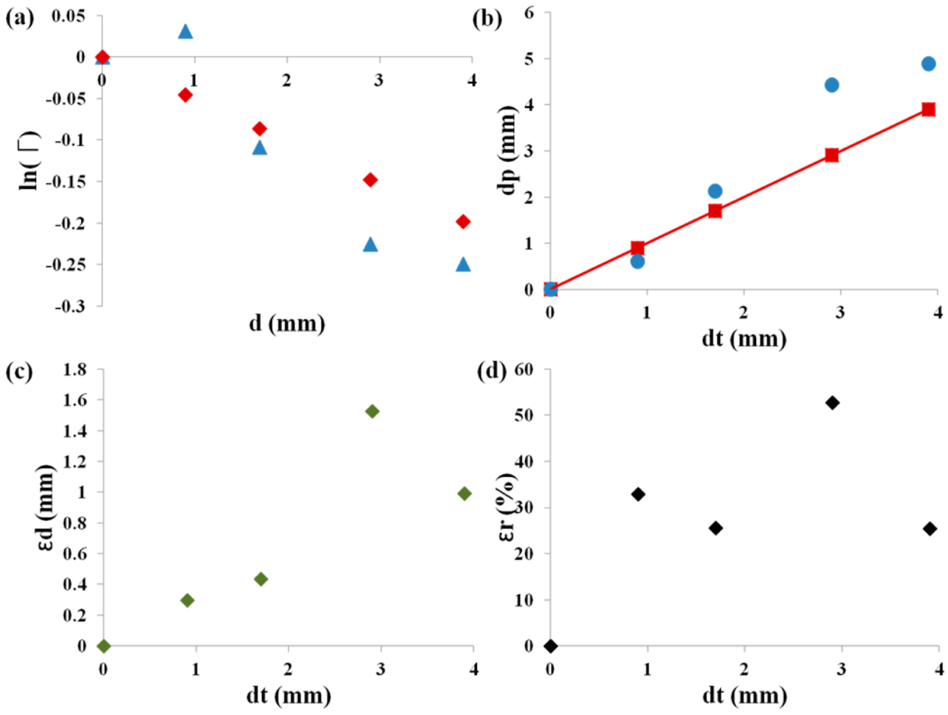

Figure 7. Comparison of theoretical predictions with experimental results for (a) Gamma values, where red rhombuses correspond to theoretical predictions and blue triangles represent experimental measurements. (b) Depth predictions, where red squares corresponding to real depth values and blue circles represent predicted depth values from experimental measurements and analytical model. (c) Absolute and (d) relative errors between predicted and real depth values, respectively.

λ_2 = 560 nm are estimated. The gamma at a given depth (d) is evaluated by the following expression

$$\Gamma^d = \frac{F^{\lambda 1}}{F^{\lambda 2}} \tag{4}$$

where F^{λ} is the average fluorescence intensity evaluated over the square ROI on images.

The theoretical slope $m = [(1/\delta^{\lambda_2}) - (1/\delta^{\lambda_1})]$ is calculated and used in combination with evaluated gamma in the form of the linear equation:

$$\ln \Gamma^d_{\text{exp}} = md \tag{5}$$

where $\Gamma^d_{\text{exp}} = (\Gamma^d/\Gamma^{d=0})$ is the gamma at a given depth (d) normalized by the gamma at 0 mm depth in order to predict the phosphor depth values (d) below the tissue as shown in Figure 7b. In addition to the minimization of the reflectance spectra from the laser and maximization of the fluorescence spectra, this normalization removes the dependence of eq 5 on diffusion constants[19] that are present in eq 1.

Overall, these results reveal significant correlation of gamma with the local source depth in subsurface imaging. These results can provide new pathways for medical diagnostics and imaging with rare-earth-doped materials.[25−29] For example, surgeons can use this approach for intraoperative resection of tumors during neurosurgery, because the brain tumor is indistinguishable from surrounding healthy brain tissue under white light illumination. This approach combined with topographic mapping of tumor depth below the healthy tissue could be very promising for accurate resection of subsurface tumor. Besides the brain tumor depth detection, this technique has the potential for depth detection of different types of tumors located below the healthy tissue. The toxicity studies of Gd_2O_2S:Yb/Er upconverting phosphors used in these studies have shown to be nontoxic in mice cells.[18] Thus, the Gd_2O_2S:Yb/Er and other variant rare-doped phosphors[30,31] are promising agents for depth resolved imaging.

3.5. Confocal Imaging Results. As a preliminary investigation of the suitability of the phosphor for bioimaging applications, fibroblast cells (L929) have been incubated with the phosphors for 24 h, stained, and imaged with a multiphoton/confocal microscope. Images of the cells are obtained by exciting the DAPI at 560 nm, the Alexa fluor at 647 nm, and the upconverting nanoparticles at 980 nm. Although the phosphors are not surface functionalized to increase cellular uptake or specific binding, it is especially useful to understand how the core nanoparticles in any such system will interact with cells since the stability of shells and polymer coatings in a biological milieu can vary. The confocal images of the cells (Figure 8a−d) clearly show that the phosphors are readily taken up by the cells. Furthermore, the nanoparticles are found to be within both the cytoplasm and the nucleus at the time of imaging. Although there is some clustering of the particles observed both inside and outside of the cells, it does not prohibit them from entering into the cells nor does it induce any significant cytotoxic response. In Figure 8, the green color shows the emission from individual phosphor particles while the yellow color is from the cluster of particles, where the emission is dominated by the red fluorescence that mixes with green to form yellow emission. The confocal results show that the upconversion emission is coming from within the cells. It also shows that some of the cells are endocytosing a large cluster of the upconverting nanoparticles.

4. CONCLUSION

We demonstrated the subsurface imaging of Gd_2O_2S:Yb/Er upconverting phosphors embedded beneath the chicken breast tissue of different depths by using the fDOT technique. We measured average emission intensities from acquired images at

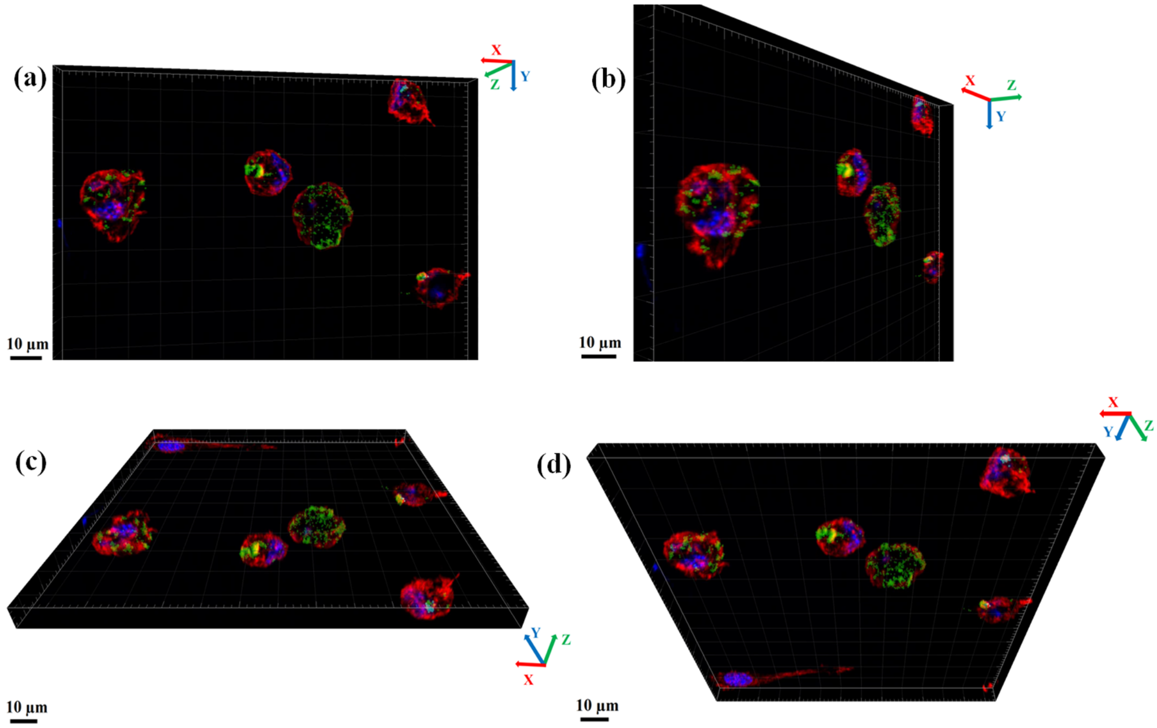

Figure 8. (a–d) Three-dimensional images obtained from the confocal images of fibroblast cells with phosphor particles. The green color corresponds to the emission from individual phosphor particles. The yellow color represents the cluster of particles, whereas the emission is dominated by the red fluorescence, which mixes with green to form yellow emission.

each depth for green wavelengths, and calculated the intensity ratio combination for these wavelengths. The results for calculated intensity ratio revealed linear correlation with depth and agreed well with theoretical predictions. In vitro tests showed no significant toxicity. The paramagnetic properties of phosphors exposed the possibility to use them for MRI imaging. The confocal imaging showed that phosphor particles can penetrate into cells, which revealed their potential for in vivo tissue imaging. Future work will require automatized measurements of images and optical properties of tissue, change of the phosphor depth, and integration of all these measurements with a computer via especially designed software. Possible applications of this approach could lead to the development of real-time intraoperative multifunational phosphor agent, which could be used during the surgeries. It could guide surgeons during the depth-resolved surgeries by providing real-time depth information on the tissue where phosphors have previously been injected and/or accumulated. In addition to that, it could provide additional MRI information, thus vastly enhancing the medical imaging capabilities.

■ AUTHOR INFORMATION

Corresponding Author

*E-mail: vkf002@my.utsa.edu.

Notes

The authors declare no competing financial interest.

Funding

Christopher Mimun acknowledges the financial support from National Institute of Health (NIGMS RISE GM060655).

■ ACKNOWLEDGMENTS

The authors thank and acknowledge the National Science Foundation Partnerships for Research and Education in Materials (NSF-PREM) Grant DMR-0934218. Chamath Dannangoda and Karen S. Martirosyan acknowledge the financial support from National Science Foundation (Grants 1126410, 1138205, and HRD-1242090) and the Department of Defense (Grant 66389-CH-REP).

■ REFERENCES

(1) Chatterjee, D. K.; Gnanasammandhan, M. K.; Zhang, Y. Small Upconversion Nanoparticles for Biomedical Applications. *Small* **2010**, *6*, 2781–2795.

(2) Nune, S. K.; Gunda, P.; Thallapally, P. K.; Lin, Y.-Y.; Laird Forrest, M.; Berkland, C. J. Nanoparticles for Biomedical Imaging. *Expert Opin. Drug Delivery* **2009**, *6*, 1175–1194.

(3) Keereweer, S.; Van Driel, P. B.; Snoeks, T. J.; Kerrebijn, J. D.; Baatenburg de Jong, R. J.; Vahrmeijer, A. L.; Sterenborg, H. J.; Löwik, C. W. Optical Image-Guided Cancer Surgery: Challenges and Limitations. *Clin. Cancer Res.* **2013**, *19*, 3745–3754.

(4) Valdés, P. A.; Leblond, F.; Jacobs, V. L.; Wilson, B. C.; Paulsen, K. D.; Roberts, D. W. Quantitative, Spectrally-Resolved Intraoperative Fluorescence Imaging. *Sci. Rep.* **2012**, *2*, 798.

(5) Medintz, I. L.; Mattoussi, H.; Clapp, A. R. Potential Clinical Applications of Quantum Dots. *Int. J. Nanomed.* **2008**, *3*, 151–167.

(6) Fernández-Suárez, M.; Ting, A. Y. Fluorescent Probes for Super-Resolution Imaging in Living Cells. *Nat. Rev. Mol. Cell Biol.* **2008**, *9*, 929–943.

(7) Pinaud, F.; Michalet, X.; Bentolila, L. A.; Tsay, J. M.; Doose, S.; Li, J. J.; Iyer, G.; Weiss, S. Advances in Fluorescence Imaging with Quantum Dot Bio-Probes. *Biomaterials* **2006**, *27*, 1679–1687.

(8) Leblond, F.; Davis, S. C.; Valdés, P. A.; Pogue, B. W. Pre-Clinical Whole-Body Fluorescence Imaging: Review of Instruments, Methods and Applications. *J. Photochem. Photobiol., B* **2010**, *98*, 77–94.

(9) Chaudhari, A. J.; Ahn, S.; Levenson, R.; Badawi, R. D.; Cherry, S. R.; Leahy, R. M. Excitation Spectroscopy in Multispectral Optical Fluorescence Tomography: Methodology, Feasibility and Computer Simulation Studies. *Phys. Med. Biol.* **2009**, *54*, 4687–4704.

(10) Zacharopoulos, A. D.; Svenmarker, P.; Axelsson, J.; Schweiger, M.; Arridge, S. R.; Andersson-Engels, S. A Matrix-Free Algorithm for Multiple Wavelength Fluorescence Tomography. *Opt. Express* **2009**, *17*, 3042−3051.

(11) Swartling, J.; Svensson, J.; Bengtsson, D.; Terike, K.; Andersson-Engels, S. Fluorescence Spectra Provide Information on the Depth of Fluorescent Lesions in Tissue. *Appl. Opt.* **2005**, *44*, 1934−1941.

(12) Svensson, J.; Andersson-Engels, S. Modeling of Spectral Changes for Depth Localization of Fluorescent Inclusion. *Opt. Express* **2005**, *13*, 4263−4274.

(13) Leblond, F.; Ovanesyan, Z.; Davis, S. C.; Valdés, P. A.; Kim, A.; Hartov, A.; Wilson, B. C.; Pogue, B. W.; Paulsen, K. D.; Roberts, D. W. Analytic Expression of Fluorescence Ratio Detection Correlates with Depth in Multi-Spectral Sub-Surface Imaging. *Phys. Med. Biol.* **2011**, *56*, 6823−6837.

(14) Leblond, F.; Ovanesyan, Z.; Davis, S. C.; Krishnaswamy, V.; Valdés, P. A.; Kim, A.; Wilson, B. C.; Hartov, A.; Pogue, B. W.; Paulsen, K. D.; Roberts, D. W. Towards Depth-Resolved Fluorescence-Guided Surgery Using Multi-Spectral Near-Infrared Light. In *Biomedical Optics and 3D Imaging, OSA Technical Digest*; Optical Society of America: Washington, D.C., 2010; paper BTuD97.

(15) Svenmarker, P.; Xu, C. T.; Liu, H.; Wu, X.; Andersson-Engels, S. Multispectral Guided Fluorescence Diffuse Optical Tomography Using Upconverting Nanoparticles. *Appl. Phys. Lett.* **2014**, *104*, 073703.

(16) Cobley, C. M.; Chen, J.; Cho, E. C.; Wang, L. V.; Xia, Y. Gold Nanostructures: a Class of Multifunctional Materials for Biomedical Applications. *Chem. Soc. Rev.* **2011**, *40*, 44−56.

(17) Cha, C.; Shin, S. R.; Annabi, N.; Dokmeci, M. R.; Khademhosseini, A. Carbon-Based Nanomaterials: Multifunctional Materials for Biomedical Engineering. *ACS Nano* **2013**, *7*, 2891−2897.

(18) Ajithkumar, G. A.; Yoo, B.; Goral, D. E.; Hornsby, P. J.; Lin, A.-L.; Ladiwala, U.; Dravid, V. P.; Sardar, D. K. Multimodal Bioimaging Using a Rare Earth Doped Gd_2O_2S:Yb/Er Phosphor with Upconversion Luminescence and Magnetic Resonance Properties. *J. Mater. Chem. B* **2013**, *1*, 1561−1572.

(19) Kolste, K. K.; Kanick, S. C.; Valdés, P. A.; Jermyn, M.; Wilson, B. C.; Roberts, D. W.; Paulsen, K. D.; Leblond, F. Macroscopic Optical Imaging Technique for Wide-Field Estimation of Fluorescence Depth in Optically Turbid Media for Application in Brain Tumor Surgical Guidance. *J. Biomed. Opt.* **2015**, *20*, 026002.

(20) Kumar, G. A.; Pokhrel, M.; Martinez, A.; Dennis, R. C.; Villegas, I. L.; Sardar, D. K. Synthesis and Spectroscopy of Color Tunable $Y_2O_2S:Yb^{3+},Er^{3+}$ Phosphors with Intense Emission. *J. Alloys Compd.* **2012**, *513*, 559−565.

(21) Burgess, A.; Vigneron, S.; Brioudes, E.; Labbé, J.-C.; Lorca, T.; Castro, A. Loss of Human Greatwall Results in G2 Arrest and Multiple Mitotic Defects Due to Deregulation of the Cyclin B-Cdc2/PP2A Balance. *Proc. Natl. Acad. Sci. U. S. A.* **2010**, *107*, 12564−12569.

(22) Marquez, G.; Wang, L. V.; Lin, S. P.; Schwartz, J. A.; Thomsen, S. L. Anisotropy in the Absorption and Scattering Spectra of Chicken Breast Tissue. *Appl. Opt.* **1998**, *37*, 798−804.

(23) Jermyn, M.; Kolste, K.; Pichette, J.; Sheehy, G.; Angulo-Rodríguez, L.; Paulsen, K. D.; Roberts, D. W.; Wilson, B. C.; Petrecca, K.; Leblond, F. Macroscopic-Imaging Technique for Subsurface Quantification of Near-Infrared Markers During Surgery. *J. Biomed. Opt.* **2015**, *20*, 036014.

(24) Mendoza, D.; Morales, F.; Walter, J. Magnetization Studies in Quasi Two-Dimensional Palladium Nanoparticles Encapsulated in a Graphite Host. *J. Phys.: Condens. Matter* **1999**, *11*, 317−322.

(25) Chatterjee, D. K.; Rufaihah, A. J.; Zhang, Y. Upconversion Fluorescence Imaging of Cells and Small Animals Using Lanthanide Doped Nanocrystals. *Biomaterials* **2008**, *29*, 937−943.

(26) Setua, S.; Menon, D.; Asok, A.; Nair, S.; Koyakutty, M. Folate Receptor Targeted, Rare-Earth Oxide Nanocrystals for bi-Modal Fluorescence and Magnetic Imaging of Cancer Cells. *Biomaterials* **2010**, *31*, 714−729.

(27) Naczynski, D. J.; Tan, M. C.; Zevon, M.; Wall, B.; Kohl, J.; Kulesa, A.; Chen, S.; Roth, C. M.; Riman, R. E.; Moghe, P. V. Rare-Earth-Doped Biological Composites as in Vivo Shortwave Infrared Reporters. *Nat. Commun.* **2013**, *4*, 2199.

(28) Sheng, Y.; Liao, L.-D.; Thakor, N.; Tan, M. C. Rare-Earth Doped Particles as Dual-Modality Contrast Agent for Minimally-Invasive Luminescence and Dual-Wavelength Photoacoustic Imaging. *Sci. Rep.* **2014**, *4*, 6562.

(29) Naccache, R.; Rodríguez, E. M.; Bogdan, N.; Sanz-Rodríguez, F.; de la Cruz, M. C. I.; de la Fuente, Á. J.; Vetrone, F.; Jaque, D.; Solé, J. G.; Capobianco, J. A. High Resolution Fluorescence Imaging of Cancers Using Lanthanide Ion-Doped Upconverting Nanocrystals. *Cancers* **2012**, *4*, 1067−1105.

(30) Pokhrel, M.; Kumar, G. A.; Balaji, S.; Debnath, R.; Sardar, D. K. Optical Characterization of Er^{3+} and Yb^{3+} co-Doped Barium Fluorotellurite Glass. *J. Lumin.* **2012**, *132*, 1910−1916.

(31) Pokhrel, M.; Mimun, L. C.; Yust, B.; Kumar, G. A.; Dhanale, A.; Tang, L.; Sardar, D. K. Stokes Emission in $GdF_3:Nd^{3+}$ Nanoparticles for Bioimaging Probes. *Nanoscale* **2014**, *6*, 1667−1674.

DOI: 10.1021/acsami.5b06491
ACS Appl. Mater. Interfaces 2015, 7, 21465−21471